

Cite this: *J. Mater. Chem. A*, 2017, 5, 12310

# Metal-free branched alkyl tetrathienoacene (TTAR)-based sensitizers for high-performance dye-sensitized solar cells†

Yamuna Ezhumalai,<sup>‡a</sup> Byunghong Lee,<sup>‡b</sup> Miao-Syuan Fan,<sup>‡c</sup> Boris Harutyunyan,<sup>‡d</sup> Kumaresan Prabakaran,<sup>‡ae</sup> Chuan-Pei Lee,<sup>c</sup> Sheng Hsiung Chang,<sup>f</sup> Jen-Shyang Ni,<sup>g</sup> Sureshraj Vagiraju,<sup>a</sup> Pragma Priyanka,<sup>a</sup> Ya-Wen Wu,<sup>a</sup> Chia-Wei Liu,<sup>a</sup> Shuehlin Yau,<sup>a</sup> Jiann T. Lin,<sup>g</sup> Chun-Guey Wu,<sup>‡af</sup> Michael J. Bedzyk,<sup>\*dh</sup> Robert P. H. Chang,<sup>\*b</sup> Ming-Chou Chen,<sup>‡\*a</sup> Kuo-Chuan Ho<sup>\*c</sup> and Tobin J. Marks<sup>‡\*i</sup>

A new series of metal-free alkylated tetrathienoacene (TTAR)-based organic chromophores, TPA–TTAR–TA (R = branched-C<sub>8</sub>H<sub>17</sub>, **1**, TTAR-b8; R = C<sub>15</sub>H<sub>31</sub>, **2**, TTAR-15; R = C<sub>9</sub>H<sub>19</sub>, **3**, TTAR-9), are synthesized for application in dye-sensitized solar cells (DSSCs). Due to the extensively conjugated TTAR  $\pi$ -bridge, all three dyes exhibit high extinction coefficients ( $1 \times 10^5 \text{ M}^{-1} \text{ cm}^{-1}$ ). By systematically exploring the effects of the TTAR alkyl chain substituents, a significant influence of the dye coverage (orientation) on the TiO<sub>2</sub> surfaces is observed. The branched-alkyl TTAR-b8 (**1**) promotes significant tilting and packing distortion on TiO<sub>2</sub> in comparison to more ordered monolayers of linear long alkyls TTAR-15 (**2**) and TTAR-9 (**3**). Photophysical measurements on the dye-grafted TiO<sub>2</sub> films reveal that the branched-alkylated TTA unit in **1** enhances the electron injection efficiency, in agreement with the high quantum efficiency. Notably, by utilizing a three-dimensional (3D) photonic crystal (PhC) layer to enhance the coherent scattering an increase the light absorption, TTAR-b8 exhibits higher short-circuit current densities and achieved a high PCE of 11.18%. TTAR-b8 is thus the best performing fused-thiophene-based organic DSSC dye reported to date.

Received 28th February 2017  
Accepted 26th April 2017

DOI: 10.1039/c7ta01825h

rsc.li/materials-a

## Introduction

Dye-sensitized solar cells (DSSCs) have attracted enormous attention in the past couple of decades, due to their ability to efficiently convert solar energy to electricity at a low cost.<sup>1</sup> The improvement in DSSCs' performance depends on the properties of the elements used in the device, such as the photosensitizer,

counter electrode, photoanode, electrolyte, and their combination. Undoubtedly, the development of more effective sensitizers is one of the most promising ways to obtain further advances in DSSCs.<sup>2–4</sup> Among the various sensitizers, porphyrin sensitizer-based DSSCs in combination with a cobalt electrolyte and platinum counter electrode show a certified PCE value of 13%.<sup>5–7</sup> However, the tedious synthesis process and low yield of porphyrin may limit the large-scale application of this sensitizer. As a result, metal-free organic dyes have attracted considerable attention for practical applications due to the following characteristics: (i) chemical versatility and facile synthesis approaches in terms of molecular tailoring; (ii) a tunable spectral property, to enable broad and high levels of solar spectral absorption in the visible region; and (iii) low production cost.<sup>8–11</sup> However, the performance of DSSCs using organic dyes remains behind that of those using metal-incorporated sensitizers, because of their lower open-circuit voltage and higher recombination rate.<sup>12–14</sup> Still, a few recent reports have reported impressive efficiencies of 10.65% and 12.5% employing single metal-free organic dyes, thus showing good potential for the future development of DSSCs.<sup>15,16</sup>

Most of the metal-free organic sensitizers employed in DSSCs consist of an electron donor and an acceptor connected by a  $\pi$ -conjugated linker, thus presenting wide possibilities for structural modification.<sup>17–20</sup> In such dye systems, triarylamine

<sup>a</sup>Department of Chemistry, National Central University, Chung-Li-32054, Taiwan. E-mail: mcchen@ncu.edu.tw

<sup>b</sup>Materials Research Institute, Northwestern University, Evanston, IL 60208, USA

<sup>c</sup>Department of Chemical Engineering, National Taiwan University, Taipei 10617, Taiwan. E-mail: kcho@ntu.edu.tw

<sup>d</sup>Department of Physics, Astronomy and the Argonne-Northwestern Solar Energy Research Center, Northwestern University, Evanston, Illinois 60208, USA

<sup>e</sup>Department of Chemistry, PSG College of Arts and Science, Coimbatore-641014, India

<sup>f</sup>Research Center for New Generation Photovoltaics, National Central University, Chung-Li 32054, Taiwan

<sup>g</sup>Institute of Chemistry, Academia Sinica, Nankang, Taipei 11529, Taiwan

<sup>h</sup>Department of Materials Science and Engineering, The Argonne-Northwestern Solar Energy Research Center, Northwestern University, Evanston, Illinois 60208, USA

<sup>i</sup>Department of Chemistry, The Materials Research Center, The Argonne-Northwestern Solar Energy Research Center, Northwestern University, Evanston, Illinois 60208, USA. E-mail: t-marks@northwestern.edu

† Electronic supplementary information (ESI) available. See DOI: 10.1039/c7ta01825h

‡ These authors contributed equally.

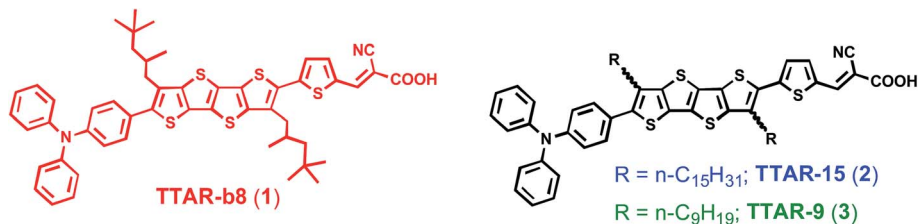


Fig. 1 Chemical structures of TTA-based dyes (1–3).

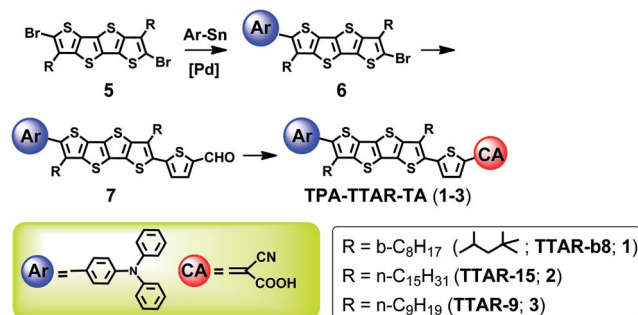
and cyanoacrylic acid are widely employed as a donor and acceptor units, respectively, and various  $\pi$ -conjugated linkers are used to bridge the donor and acceptor units to create a diverse range of D- $\pi$ -A dyes for DSSCs.<sup>21–23</sup> It is well known that the  $\pi$ -spacer plays an important role in tuning the molecular band gap, while electronic and steric factors also have strong impacts on device performance. For these reasons we have been interested in implementing the unique planar conjugated tetrathienoacene (TTA) framework in DSSCs, since it exhibits excellent hole/electron mobility in organic thin film transistors (OTFTs) due to long range order and favorable reorganization energies.<sup>24,25</sup> Following its successful application in OTFTs and two-photon processing, it was recently investigated as a bridge to construct D- $\pi$ -A organic DSSC dyes, and achieved a device power conversion efficiency (PCE) of 10.1% with dye **TTAR-15** (Fig. 1).<sup>26</sup> The linear C15-alkyl chain substituent not only prevents dye aggregation, but also curtails charge recombination. However, it does not efficiently suppress intermolecular  $\pi$ - $\pi$  interactions when the molecules assemble on the  $\text{TiO}_2$  surface.

Therefore, to enhance the effectiveness of the TTA unit as a charge transporting  $\pi$ -linker and increase the  $V_{\text{OC}}$  by suppressing close intermolecular  $\pi$ - $\pi$  interactions, we designed and synthesized a new sensitizer functionalized with a branched alkyl group ( $\text{b-C}_8\text{H}_{17}$ ), **TTAR-b8** (1). To examine the effects on the short-circuit current density ( $J_{\text{SC}}$ ) at higher dye coverages, the **TTAR-15** C15 linear alkyl chain was also changed to C9. Therefore, the linear alkyl chain ( $\text{C}_{15}\text{H}_{31}$  and  $\text{C}_9\text{H}_{19}$ ) substituted dye molecules **TTAR-15** (2) and **TTAR-9** (3) (Fig. 1) were prepared for this detailed comparative study. The effects of the branched alkyl chains vs. linear chains TTARs on photovoltaic performance and charge recombination dynamics in DSSCs are fully investigated.

## Results and discussion

### Design and synthesis of TTA sensitizers

Two new organic dye molecules were constructed using our recently published methodology for the high-performance TTA dyes, exemplified by **TPA-TTAR-TA**.<sup>26</sup> The stepwise synthesis is illustrated in Scheme 1. The soluble alkylated dibromotetrathienoacenes (5) were first mono-coupled with the triphenyl amino-donor moiety to produce the mono-brominated tetrathienoacenes, 6 (a–c), which were then coupled with 5-(1,3-dioxolan-2-yl)thiophen-2-yltributylstannane via Stille coupling to yield the corresponding aldehydes 7 (a–c). These



Scheme 1 Synthetic routes to metal-free DSSC sensitizers 1–3.

were then treated with cyanoacetic acid in the presence of piperidine to produce dyes 1–3. The alkylated dibromotetrathienoacenes (5) were prepared by bromination of the alkylated TTA core (4) with *N*-bromosuccinimide. Alkylated tetrathienoacenes were then prepared by acylation of the tetrabromothiopheno[3,2-*b*]thiophenes and cyclization with 2-mercaptoacetate, followed by hydrolysis and decarboxylation. Detailed synthetic procedures and analytical data are provided in the ESI.†

### Optical, electrochemical data, and DFT calculations

The UV-vis absorption spectra of three sensitizers in *o*- $\text{C}_6\text{H}_4\text{Cl}_2$  solutions ( $1 \times 10^{-5}$  M) are shown in Fig. 2a. The spectra of dyes 1–3 show the presence of two strong absorptions assignable to charge-transfer (CT) bands at  $\lambda_{\text{max}} \sim 485$  nm (1),  $\sim 498$  nm (2),  $\sim 519$  nm (3), and a higher energy  $\pi$ - $\pi^*$  transition at  $\lambda_{\text{max}} \sim 373$  nm (1),  $\sim 378$  nm (2),  $\sim 375$  nm (3). These almost identical absorption maxima are straightforward to explain, since these three dyes have similar chemical structures except for the three different alkyl substituents. Compared to **TTAR-15** ( $\lambda_{\text{max}} \sim 498$  nm), the introduction of a branched alkyl chain into the TTA framework blue-shifts the ICT absorption peak by  $\sim 13$  nm.<sup>27</sup> **TTAR-b8** has a greater molar extinction coefficient than **TTAR-15** and **TTAR-9**. Presumably the reduced molecular co-planarity of **TTAR-b8** due to the branched alkyl substituents may perturb the conjugation efficiency of the chromophore, and hence hypsochromically shift the absorption maximum wavelength. This is in line with the results of the DFT calculations (*vide infra*). All the dyes adsorbed on the  $2.57 \pm 0.07$   $\mu\text{m}$ -thick  $\text{TiO}_2$  thin film exhibit red-shifted absorption profiles (Fig. 2b) in comparison to that measured in the solution. The red-shifted

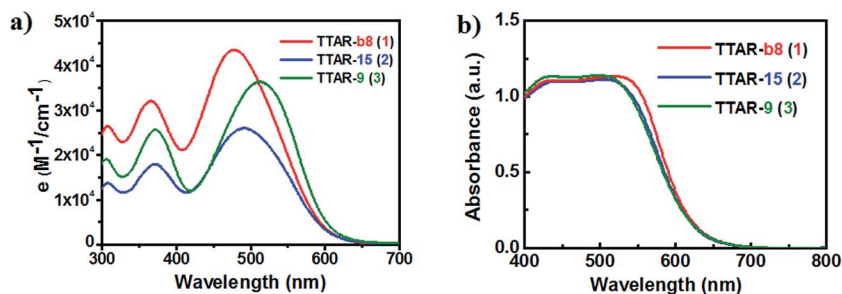


Fig. 2 Absorption spectra of the dyes (a) measured in *o*-C<sub>6</sub>H<sub>4</sub>Cl<sub>2</sub> solution in a concentration of 10<sup>-5</sup> M and (b) dye-sensitized nanocrystalline TiO<sub>2</sub> films.

absorption may be attributed to the intermolecular interactions on the TiO<sub>2</sub> surface, which are likely to occur due to the presence of a TiO<sub>2</sub> layer.

To investigate the substitution effects on the TTA molecular energy levels, the electrochemical properties of these dyes were analyzed by differential pulse voltammetry (DPV) in 1,2-dichlorobenzene solutions with 0.1 M tetrabutylammonium hexafluorophosphate (TBAPF<sub>6</sub>) as the electrolyte, and a three-electrode configuration consisting of a Pt disk working electrode, an auxiliary Pt wire electrode, and a nonaqueous Ag reference electrode. All potentials reported are referenced to a Fc<sup>+</sup>/Fc internal standard (at +0.6 V). The DPVs of the oxidation peaks of 1–3 are exhibited at 0.99, 0.99 and 1.00 (V), respectively, as shown in Table 1. As shown in Fig. 3, all three dyes exhibit the first oxidative peaks ( $E_{\text{ox}}$ ) around +0.99 V, and thus the HOMO energies of the three dyes are estimated around -5.19 eV, using  $E_{\text{HOMO}} = -(4.2 + E_{\text{ox}})$ ; assuming ferrocene/ferrocenium oxidation at -4.8 eV. Extracted from the optical absorption spectra, the LUMO energies ( $E_{\text{LUMO}} = E_{\text{HOMO}} + \Delta E_{\text{g}}$ ) of the three dyes were calculated as approximately ~3.28 eV.<sup>28</sup> Since dye 1 had the most blue-shifted optical absorption spectrum it also has the highest LUMO energy, as shown in Fig. 4, indicating reduced conjugation in agreement with the results of the DFT calculations (*vide infra*).

Electronic structure calculations were performed at the B3LYP/6-31G\* level of density functional theory. The electronic distribution of the calculated frontier molecular orbitals and the DFT derived HOMO and LUMO values are shown in Fig. 4b, while the optimized molecular structures and intramolecular dihedral angles are shown in Fig. 4c. Fig. 4b shows the HOMO and LUMO topologies for dyes 1–3 (Table 1), indicating that the

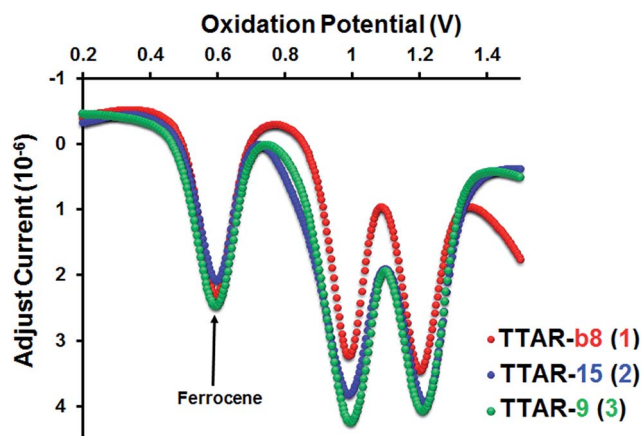


Fig. 3 DPV oxidation potential curves of dyes 1–3 in *o*-C<sub>6</sub>H<sub>4</sub>Cl<sub>2</sub> solution.

HOMOs are localized primarily at the TPA donor moieties and extend to the conjugated TTA core, while the LUMOs are primarily localized on the cyanoacrylic acid unit.<sup>29</sup> Such a directional electronic distribution is ideal for electron injection into TiO<sub>2</sub> from dye anchoring sites and reduction of oxidized dyes by I<sup>-</sup>/I<sub>3</sub><sup>-</sup>.<sup>21</sup> The computed HOMO energies are -4.99, -4.99, and -5.02 eV for 1–3, respectively, and the excited state (LUMO) energies are uniformly -2.71 eV for 1–3. Note that the DFT computed HOMO–LUMO energy gaps of three dyes are in excellent agreement with those values obtained from DPV measurements (*vide supra*). As shown in Fig. 4c, the dihedral angles indicate less coplanarity in 1 (50.5° + 20.1°) versus 2 (43.5° + 14.2°) and 3 (44.5° + 17.2°), indicating that compound 1

Table 1 Optical and electrochemical properties of TTA dyes

Dye	UV-vis <sup>a</sup> $\lambda_{\text{max}}$ (nm)	$\Delta E_{\text{g}}$ (eV) (UV) <sup>b</sup>	$E_{\text{ox}}$ <sup>c</sup> (V)	Energy level (eV)		Energy level (eV)	
				$E_{\text{HOMO}}$ <sup>d</sup>	$E_{\text{LUMO}}$ <sup>e</sup>	$E_{\text{HOMO}}$ <sup>f</sup>	$E_{\text{LUMO}}$ <sup>f</sup>
TTAR-b8	485	1.92	0.99	-5.19	-3.27	-5.02	-2.71
TTAR-15	498	1.91	0.99	-5.19	-3.28	-4.99	-2.71
TTAR-9	519	1.91	1.00	-5.20	-3.29	-4.99	-2.71

<sup>a</sup> In *o*-C<sub>6</sub>H<sub>4</sub>Cl<sub>2</sub> at 25 °C. <sup>b</sup> Calculated from optical absorption onset. <sup>c</sup>  $E_{\text{ox}}$  = oxidative potential, by DPV in *o*-C<sub>6</sub>H<sub>4</sub>Cl<sub>2</sub> at 25 °C, ferrocene/ferrocenium was used as the internal standard and set at +0.6 V (-4.8 eV). <sup>d</sup>  $E_{\text{HOMO}} = -(4.2 + E_{\text{ox}})$ . <sup>e</sup> Estimated from  $E_{\text{HOMO}} + \Delta E_{\text{g}}$ . <sup>f</sup> By DFT calculation.

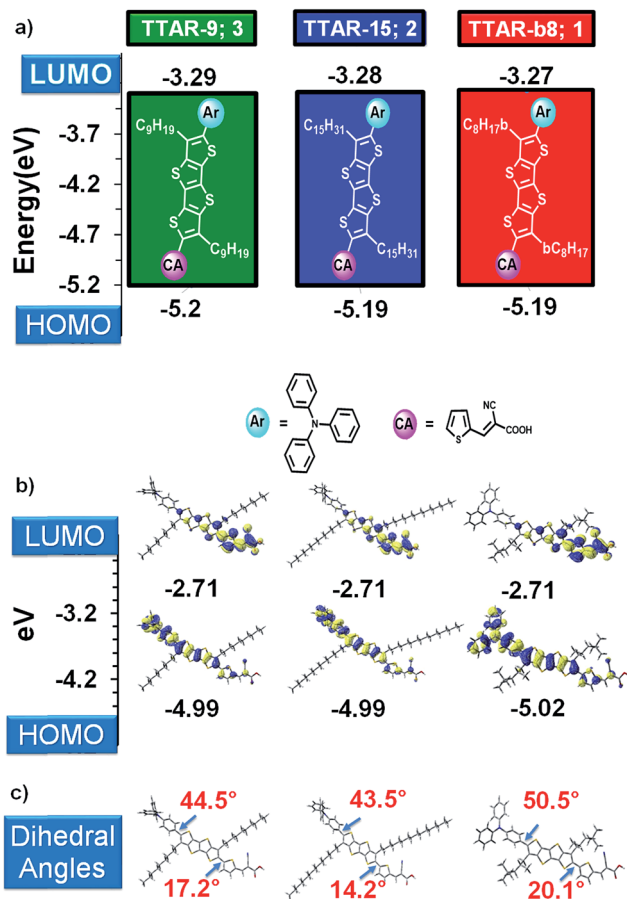


Fig. 4 Energetic alignment of molecules 1–3. (a) DPV-derived HOMO and LUMO energy levels; (b) DFT derived molecular orbitals; (c) optimized molecular structures with dihedral angles.

has less conjugation, which is in good agreement with the electrochemically and optically derived data.

The photovoltaic performances of the DSSCs with these dyes were measured under the irradiation of AM 1.5 G (100 mW cm<sup>-2</sup>) simulated solar light, and the results are plotted in Fig. 5. The corresponding parameters are summarized in Table 2. The DSSCs fabricated with **TTAR-b8** show the best results among the three dyes, with a short-circuit current density ( $J_{SC}$ ) of 17.45 mA cm<sup>-2</sup>, an open-circuit voltage ( $V_{OC}$ ) of 0.81, a fill factor (FF) of 0.72, and a cell efficiency ( $\eta$ ) as high as 10.21%, while **TTAR-9**

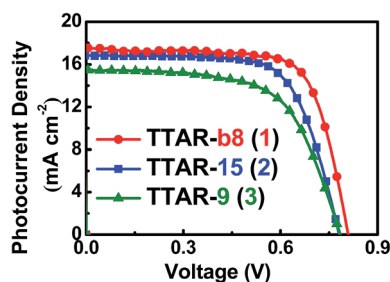


Fig. 5 The photocurrent current density–voltage ( $J$ – $V$ ) characteristics of the DSSCs with various dyes, measured under 1 sun illumination.

Table 2 Photovoltaic parameters of the DSSCs with various dyes<sup>a</sup>

Dyes	$\eta$ (%)	$V_{OC}$ (V)	$J_{SC}$ (mA cm <sup>-2</sup> )	FF
<b>TTAR-b8</b>	10.21 ± 0.17	0.81 ± 0.01	17.54 ± 0.05	0.72 ± 0.01
<b>TTAR-15</b>	9.02 ± 0.06	0.78 ± 0.01	16.86 ± 0.17	0.69 ± 0.01
<b>TTAR-9</b>	7.60 ± 0.07	0.78 ± 0.01	15.54 ± 0.06	0.62 ± 0.01

<sup>a</sup> All values obtained from three cells.

and **TTAR-15** provide relatively low  $\eta$  values of 7.60% and 9.02%, respectively. The superior performance of the cell based on dye **TTAR-b8** reflects the higher  $J_{SC}$ , attributable to the better light absorption characteristics of **TTAR-b8**. On the other hand, this higher  $J_{SC}$  of the **TTAR-b8**-sensitized cell could also be explained by the relatively lower aggregation of the dye due to the bulky 3-methyl-5,5-dimethylhexyl substituents. The **TTAR-b8**-sensitized cell was also subjected to an at-rest long-term stability test, as shown in the ESI (Fig. S1†). At the end of 20 days, the normalized cell efficiency with **TTAR-b8** maintains up to 97% of its initial value, indicating the reasonable stability of the **TTAR-b8**-sensitized cell.

Fig. 6 shows the incident photon-to-electron conversion efficiency (IPCE) spectra for the DSSCs fabricated with these three dyes. The IPCE spectra broaden and extend to 700 nm, which is consistent with the UV-vis absorption spectra of the dye-sensitized TiO<sub>2</sub> films. The broadening of the IPCE spectra is associated with larger photocurrents,<sup>30</sup> consistent with the higher  $\eta$  observed for the TTAR-series dyes.

One way to enhance the cell efficiency without altering the architecture of the conventional DSSC design is to ensure all of the photons that enter the cell are efficiently transformed into useful charges. As light traverses the cells, significant portions of the photon flux are not absorbed by the dye molecules, and cell efficiency can thus be increased by capturing the lost photons. In order to improve the conversion efficiency of the solar cell, we simply attach a reflector to the back of the cell (the cathode electrode) using a stack of the photonic crystals (Fig. 7a). As seen in this illustration, there are two physical mechanisms by which wave optics approaches (based on reflector and photonic crystals) can improve light-trapping: reflection and diffraction. A photonic crystal can reflect light incident from any angle for frequencies and polarizations within the photonic crystal, in that it can reflect light within the

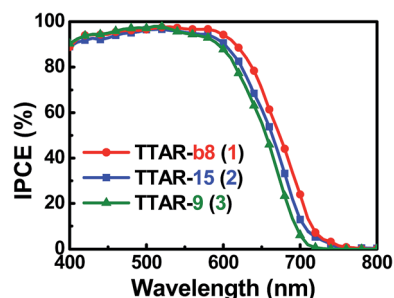


Fig. 6 IPCE plots of the DSSCs with various dyes.

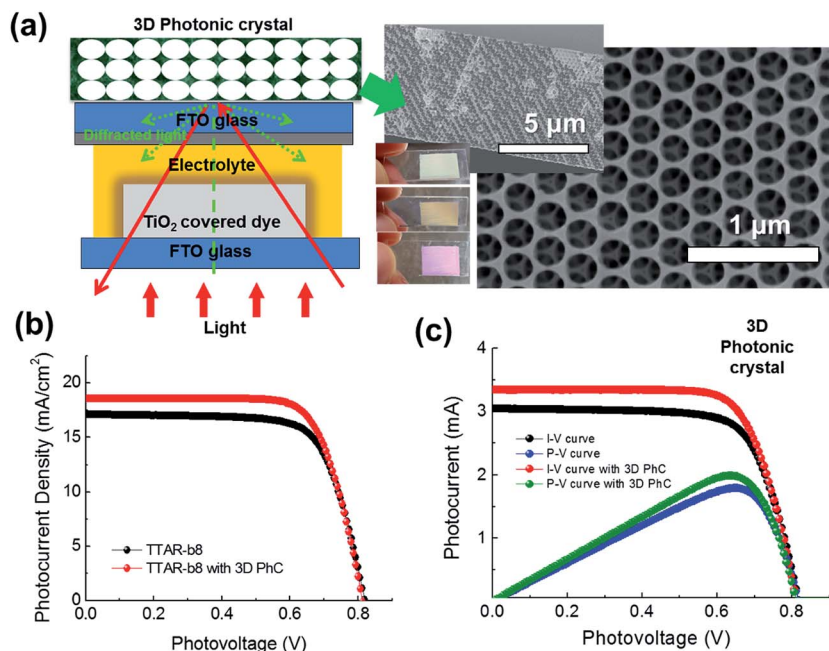


Fig. 7 (a) Configuration of the cell with the 3-D photonic crystals (the insets show photographic- and SEM images of 3D PhC); (b) and (c) the photocurrent current density–voltage ( $J$ - $V$ ) and photocurrent–voltage ( $I$ - $V$ ) with power–voltage ( $P$ - $V$ ) characteristics of the DSSCs with TTAR-b8 and 3D PC under 1 sun illumination.

bandgap incident from any angle or medium. Second, wave optics-based devices, such as surface grating and 3D PhC, can be designed to diffract incoming beams into highly oblique angles according to Bragg's law.<sup>31</sup> The diffraction induced by an interface improves light trapping by increasing the distance that light must travel to return to the front surface of the cell. Therefore, a double-layer three-dimensional (3D) photonic crystal (PhC) with a hole diameter of 375/410 nm was placed behind the count electrode to efficiently reflect and diffract the transmitted photons back into the cell for further conversion.<sup>32,33</sup> The photovoltaic performance of the **TTAR-b8** dye DSSC with a 3D PhC layer was measured under AM 1.5 G irradiation ( $100 \text{ mW cm}^{-2}$ ) simulated solar light, and the results are plotted in Fig. 7. Performance parameters are summarized in Table 3.

Electrochemical impedance spectroscopy (EIS) was next performed under dark conditions to understand the differences in  $V_{OC}$  for the cells sensitized by the present dyes (Fig. 8). In general, the Nyquist plots show three semicircles, which are assigned to electrochemical reactions at the Pt/electrolyte interface, charge transfer at the  $\text{TiO}_2$ /dye/electrolyte interface, and Warburg diffusion processes ( $\text{I}^-/\text{I}_3^-$ ) in the electrolyte. In the present DSSCs, only two semicircles are observed. It is

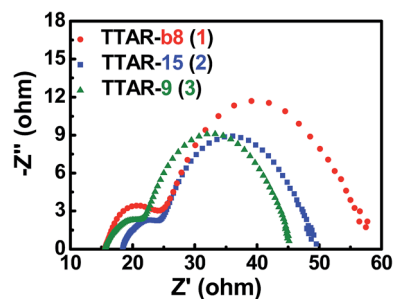


Fig. 8 Nyquist plots of the DSSCs with various dyes, measured under dark conditions.

therefore assumed that in these DSSCs the conventional diffusion resistance of the redox couple overlaps with the charge-transfer resistance, because of the relatively short length available for  $\text{I}^-$  diffusion with the thin spacer, and owing to the low viscosity of the electrolyte solvents. EIS analysis of the DSSCs was performed over the frequency range of 10 mHz to 65 kHz under dark conditions at an applied bias set at  $-0.85 \text{ V}$ . The radius of the larger semicircle and the corresponding extracted  $R_{rec}$  value increase in the order, **TTAR-9** < **TTAR-15** < **TTAR-b8**, consistent with the observed increase in  $V_{OC}$  for these DSSCs based on the TTAR-series dyes. A smaller  $R_{rec}$  value is indicative of faster exciton recombination, and may result in a comparatively small  $V_{OC}$ s.<sup>34,35</sup> Aggregation of the dyes is reported to increase recombination rates and thus reduce the  $V_{OC}$ . Upon illumination at  $100 \text{ mW cm}^{-2}$  under open-circuit conditions, the radius of the intermediate-frequency semicircle in the Nyquist plot (Fig. 9a), and hence the charge-transport resistance

Table 3 Photovoltaic parameters of the DSSCs with TTAR-b8 and 3D PC under 1 sun illumination

Compound	$V_{OC}$ (V)	$J_{SC}$ ( $\text{mA cm}^{-2}$ )	FF (%)	EFF (%)
<b>TTAR-b8</b>	0.817	17.12	71.96	10.08
<b>TTAR-b8 with 3D PhC</b>	0.811	18.79	73.31	11.18

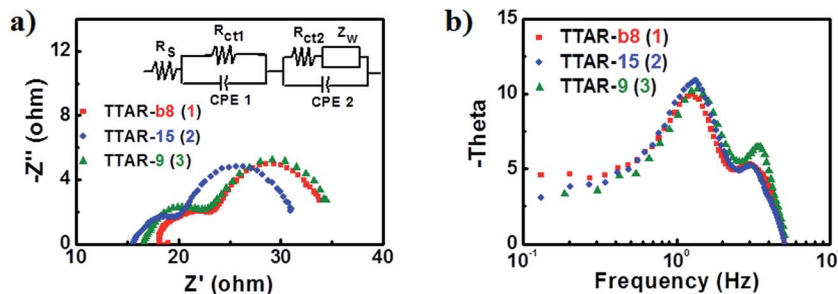


Fig. 9 (a) Nyquist and (b) Bode plots of the DSSCs with various dyes, measured under 1 sun illumination.

( $R_{ct2}$ ), follows the order **TTAR-b8** < **TTAR-15** < **TTAR-9**. Lower values of the charge-transfer resistance should favor enhanced electron collection, and thus would play an important role in increasing cell efficiency.

The electron lifetimes calculated from Bode plots (Fig. 9b) further support the ordering of  $V_{OC}$  in these cells. The Bode plots of the EIS spectra show the frequency peaks of the charge transfer process at different interfaces for cells with the different dyes. The electron lifetime ( $\tau_e$ ) for recombination in a DSSC is determined by the  $f_{max}$  value,<sup>36</sup> where  $\tau_e = (2\pi f_{max})^{-1}$  and the results are shown in Table 4. The electron lifetimes measured for the dyes **TTAR-b8**, **TTAR-15**, and **TTAR-9** are 8.69, 7.39, and 6.74 ms, respectively. The increase in electron lifetime for the **TTAR-b8**-based cell indicates the more effective suppression of the back reaction of the injected electrons with the  $I_3^-$  in the electrolyte, by alteration of the sensitizer HOMO, leading to increased photocurrent and photovoltage, hence to substantially enhanced  $\eta$ .

Dye aggregation on the surface of  $TiO_2$  generally reduces the electron lifetime and facilitates charge recombination in DSSCs fabricated using metal-organic or organic dyes.<sup>37</sup> To examine the possibility of dye aggregation, DSSCs were fabricated with various amounts of chenodeoxycholic acid (CDCA) co-adsorbed on the photoanodes. The effects of CDCA concentration on the photovoltaic properties of the DSSCs fabricated with **TTAR-b8** were first investigated, and the results are shown in Fig. 10. The corresponding photovoltaic parameters are listed in Table 5. Although dye aggregation should be suppressed by CDCA incorporation among the dye molecules, this would also decrease the dye coverage on the  $TiO_2$ . Note that the  $\eta$  of the **TTAR-b8**-based DSSCs decreases significantly with CDCA addition (Table 5). The bulky 3-methyl-5,5-dimethylhexane substituent on **TTAR-b8** may be sufficient to suppress aggregation, and adsorption of the added CDCA may compete with dye adsorption on the  $TiO_2$ . Further evidence is found in the EIS data, and all extracted values are listed in Table 6. Fig. 11 shows the

Nyquist plots of **TTAR-b8**-based DSSCs with various CDCA concentrations, measured under dark conditions. The radius of this semicircle follows the same order, which indicates that dyes based on different concentrations of CDCA possess similar charge-recombination resistances. Upon illumination at 100  $mW\ cm^{-2}$  under open-circuit conditions, the radii of the

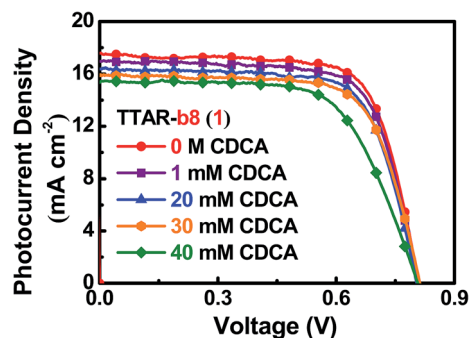


Fig. 10 The photocurrent density–voltage ( $J$ – $V$ ) characteristics of the DSSCs using **TTAR-b8** dye with various CDCA concentrations, measured under 1 sun illumination.

Table 5 Photovoltaic parameters of the DSSCs using **TTAR-b8** dye with various CDCA concentrations<sup>a</sup>

CDCA	$\eta$ (%)	$V_{OC}$ (V)	$J_{SC}$ ( $mA\ cm^{-2}$ )	FF
0 M	10.21 ± 0.17	0.81 ± 0.01	17.54 ± 0.05	0.72 ± 0.01
$1 \times 10^{-3}$ M	9.83 ± 0.12	0.80 ± 0.01	16.97 ± 0.08	0.72 ± 0.00
$10 \times 10^{-3}$ M	9.37 ± 0.06	0.80 ± 0.01	16.40 ± 0.05	0.71 ± 0.01
$20 \times 10^{-3}$ M	9.13 ± 0.15	0.81 ± 0.01	15.98 ± 0.04	0.70 ± 0.01
$30 \times 10^{-3}$ M	8.12 ± 0.15	0.81 ± 0.01	15.39 ± 0.05	0.65 ± 0.01

<sup>a</sup> Values obtained from three cells.

Table 6 Electrochemical parameters of the DSSCs using **TTAR-b8** dye with various CDCA concentrations

CDCA	$R_{rec}$ (ohm)	$R_{ct2}$ (ohm)	$f_{max}$ (Hz)	$\tau_e$ (ms)
0 M	35.95	14.27	18.31	8.69
$1 \times 10^{-3}$ M	34.27	14.94	18.31	8.69
$10 \times 10^{-3}$ M	31.97	15.12	18.31	8.69
$20 \times 10^{-3}$ M	34.02	17.48	18.31	8.69
$30 \times 10^{-3}$ M	34.53	19.38	17.96	8.86

Table 4 Electrochemical parameters of the DSSCs with various dyes

Dyes	$R_{rec}$ (ohm)	$R_{ct2}$ (ohm)	$f_{max}$ (Hz)	$\tau_e$ (ms)
<b>TTAR-b8</b>	35.95	14.27	18.31	8.69
<b>TTAR-15</b>	27.59	14.59	21.54	7.39
<b>TTAR-9</b>	27.42	15.72	23.60	6.74

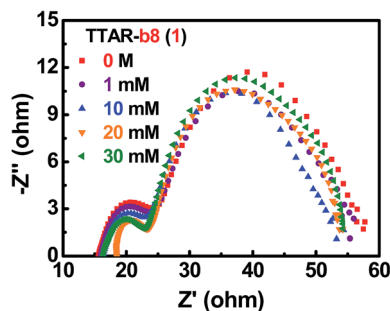


Fig. 11 Nyquist plots of the DSSCs using TTAR-b8 dye with various CDCA concentrations, measured under dark conditions.

intermediate-frequency semicircles in the Nyquist plots (Fig. 12a) indicate that the electron-transport resistance ( $R_{ct2}$ ) parallels the [CDCA] order  $0.0\text{ M} < 1\text{ mM} < 10\text{ mM} < 20\text{ mM} < 30\text{ mM}$ . Moreover, the electron lifetimes can be extracted from the angular frequency ( $\omega_{\min}$ ) at the mid-frequency peak in the Bode phase plots (Fig. 12b). The  $\tau_e$  values obtained for all cells with or without added CDCA are almost identical (Table 6).

### Broad band FTR-PL

Femtosecond time-resolved photoluminescence (FTR-PL) is a powerful tool for elucidating exciton dynamics in solution phase dyes or those adsorbed on  $\text{TiO}_2$  nanoparticle films. The lifetimes of photo-excited excitons for the present TTAR dyes were next measured using broadband femtosecond time-resolved photoluminescence spectroscopy.<sup>38</sup> The dyes dissolved in solution exhibit red-shifted PL (Fig. 13), which indicates the relaxation of the molecular structure in the excited state. To obtain the lifetimes of the photoexcited excitons in the solution phase dyes, the time-dependent PL curves were fitted with a three-exponential decay function.<sup>26</sup> The three derived time constants are listed in Table 7. In general, longer exciton lifetimes correspond to higher IPCEs. However, note that the trend in exciton lifetimes for the three dyes does not track the IPCEs at  $\lambda = 420\text{ nm}$ . To understand the extremely high IPCEs, the FTR-PLs of dyes adsorbed on  $\text{TiO}_2$  nanoparticle films was also examined. Fig. 14 presents the PL dynamics at the emission maxima. A three-exponential decay function was used to fit the PL dynamics in order to obtain the time constants for dye molecules adsorbed on  $\text{TiO}_2$  nanoparticles film.<sup>26</sup> The electron

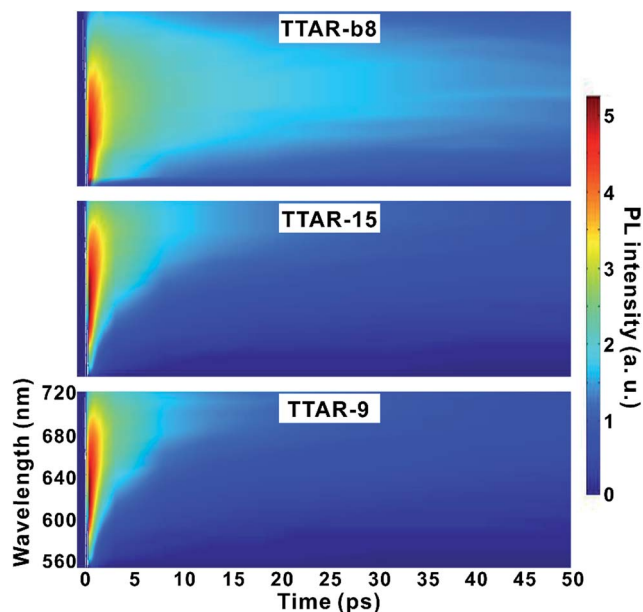


Fig. 13 Broadband time-resolved photoluminescence spectra of TTAR-b8, TTAR-15, and TTAR-9 dyes.

Table 7 Time constants of excited electrons in dyes.  $\tau_1$ ,  $\tau_2$ , and  $\tau_3$  are the exciton–exciton annihilation time, time for molecular structure relaxation, and exciton lifetime, respectively

Dye	$\tau_1$ (ps)	$\tau_2$ (ps)	$\tau_3$ (ps)
TTAR-b8	1.49	18.35	172
TTAR-15	1.54	10.90	102
TTAR-9	1.28	7.59	86

injection efficiency can be evaluated by the relationship,  $\eta = (1/\tau_1)/(1/\tau_2 + 1/\tau_3)$ , where  $\tau_1$  is the electron injection time from the dye to  $\text{TiO}_2$ ,  $\tau_2$  is the exciton–exciton annihilation time, and  $\tau_3$  is the lifetime of an exciton in the dye. The extracted time constants and electron injection efficiencies for the dye/ $\text{TiO}_2$  combinations are summarized in Table 8. For the three dyes adsorbed on the  $\text{TiO}_2$  nanoparticle films, the electron injection efficiencies from the dye to  $\text{TiO}_2$  nanoparticles are greater than 97% at  $\lambda = 420\text{ nm}$ , which is consistent with the extremely high IPCEs (>93%) at  $\lambda = 420\text{ nm}$ .

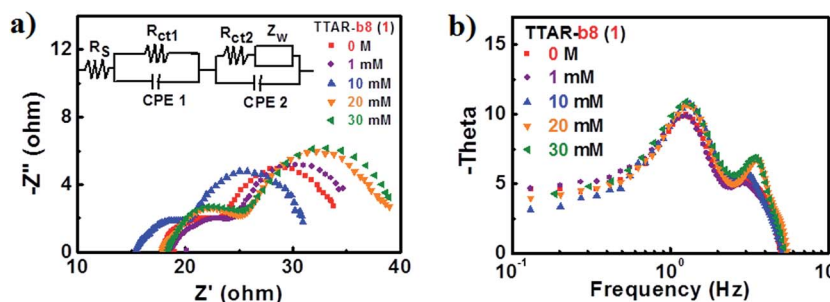


Fig. 12 (a) Nyquist and (b) Bode plots of the DSSCs using TTAR-b8 dye with various CDCA concentrations, measured under 1 sun illumination.

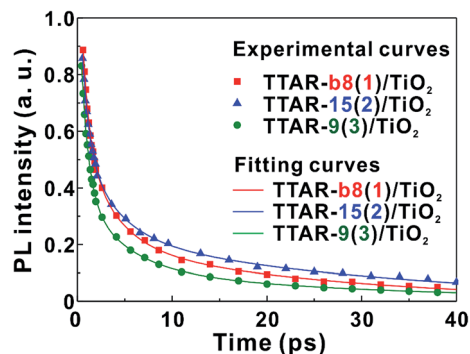


Fig. 14 FTR-PL spectra of TTAR-b8, TTAR-15, and TTAR-9 dyes.

Table 8 Time constants of excited electron and electron injection efficiency in dye/TiO<sub>2</sub>

Dye	Electron injection time (ps)	Exciton–exciton annihilation time (ps)	Exciton lifetime (ps)	Electron injection efficiency (%)
TTAR-b8/TiO <sub>2</sub>	0.71	3.37	24.74	97.2
TTAR-15/TiO <sub>2</sub>	0.73	3.61	30.31	97.7
TTAR-9/TiO <sub>2</sub>	0.77	4.59	29.86	97.5

#### Dye layer/TiO<sub>2</sub> morphology by X-ray reflectivity (XRR).

For the XRR studies, 20 Å TiO<sub>2</sub> thin films with flat (low-roughness) surfaces were grown on piranha-cleaned Si/SiO<sub>2</sub> wafers by atomic layer deposition (TDMAT + H<sub>2</sub>O). The resulting films were then dipped in 0.3 mM solutions of the three

separate dyes dissolved in DCM : ACN : *t*-butanol = 8 : 1 : 1 for 24 h with subsequent washing with ACN and drying under a UHP N<sub>2</sub> stream.<sup>39</sup> XRR  $\theta - 2\theta$  scans were performed on a Rigaku Smartlab instrument with Cu K $\alpha$  radiation of wavelength  $\lambda = 1.541$  Å. Fig. 15a shows normalized XRR data as a function of momentum transfer  $q = 4\pi \sin \theta / \lambda$  along with best fitting curves based on Parratt's recursion formulation for a slab model.<sup>40</sup> The electron density profiles for each of the model fits are shown in Fig. 15b. Table 9 and 10 list the structural parameters of the dye films inferred from the XRR analysis.

Inspection of the XRR curves clearly indicates qualitative differences between the adsorbed branched-alkyl dye **TTAR-b8** dye and the two dyes with *N*-alkyl substituents, **TTAR-15** and **TTAR-9**. The latter have comparable molecular footprints, thicknesses equal to their molecular backbone lengths, and similar density profiles. Therefore, to occupy the same space the C15 tail must favor a more compact packing than the C9 dye, leading to greater distortions of the face-to-face stacking of the fused aromatic rings and thus less likelihood of pores in the dye monolayer. This morphology also manifests itself in a less pronounced head separation for **TTAR-15**. Such steric hindrance may decrease the excitation quenching probability on neighboring molecules and recombination by charge transfer through pores in the dye monolayer. In contrast, the **TTAR-b8** molecules are significantly tilted (angle with the surface normal  $\sim 60^\circ$ ). XRR data fitting indicates a residual sparse second layer that is not removed by washing with pure solvent. This second layer shows a 10% estimated surface coverage, and is presumably a result of lateral inhomogeneity in the film, *e.g.* due to the formation of patches (islands) or other forms of aggregation which manifest in the inferred electron density

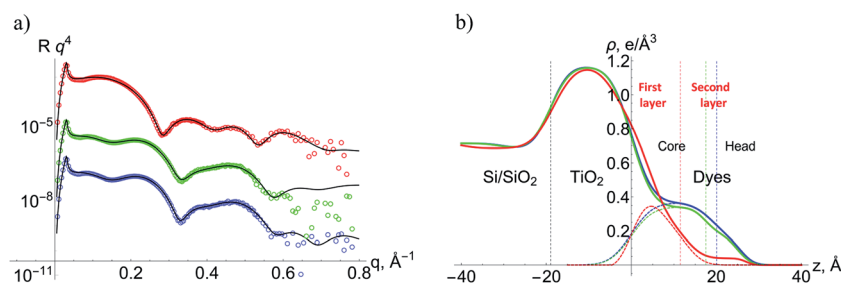


Fig. 15 (a) XRR experimental curves (circles, red—TTAR-b8, green—TTAR-9, blue—TTAR-15) and best-fitting curves (solid black lines). (b) Electron density profiles determined from the fits. Dashed lines indicate the density profiles of the dye layers after subtracting the TiO<sub>2</sub> profile (the red dashed line is for the layer adjacent to TiO<sub>2</sub>).

Table 9 Dye layer parameters inferred from XRR determined electron density profiles

Dye	Overall weighted thickness, Å	Head thickness, Å	Core thickness, Å	Head electron density, e Å <sup>-3</sup>	Core electron density, e Å <sup>-3</sup>	Air/head interface roughness, Å
TTAR-b8 <sup>a</sup>	27.0	15.4	11.6	0.04	0.35	$\sim 1.5^b$
TTAR-15	25.3	5.3	20	0.20	0.37	2.3
TTAR-9	24.8	7.3	17.5	0.18	0.34	2.6

<sup>a</sup> Core here refers to the first layer, and head to the second sparse layer. <sup>b</sup> Not reliable.

Table 10 Dye layer parameters inferred from XRR determined electron density profiles

Dye	Head/core interface roughness, Å	Core/TiO <sub>2</sub> interface roughness, Å	TiO <sub>2</sub> thickness, Å	Molecular footprint, Å <sup>2</sup>
TTAR-b8 <sup>a</sup>	3.8	4.1	19.0 <sup>b</sup>	118
TTAR-15	4.0	4.0	19.0	74
TTAR-9	2.5	4.0	19.0	67

<sup>a</sup> Core here refers to the first layer, and head to the second sparse layer. <sup>b</sup> Extrapolated from separate experiments.

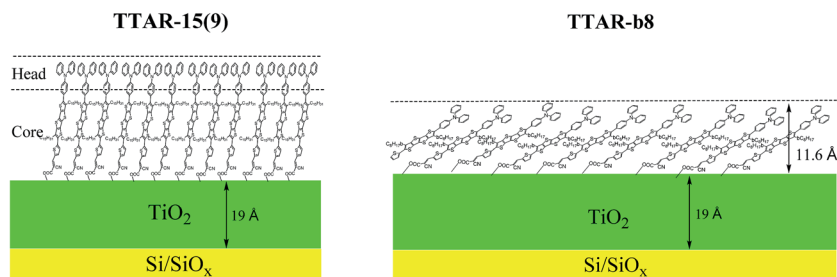


Fig. 16 Schematic depictions of plausible models conforming to the deduced parameters and XRR determined profiles from Fig. 15b for TTAR-15 (TTAR-9) and TTAR-b8.

profile as a sparse layer because of lateral averaging (Fig. 16). The head group in the first denser layer is not distinguishable in the electron density profile. These characteristics indicate a much stronger tendency for intermolecular hydrophobic attraction and a much higher level of face-to-face stacking distortion *versus* both TTAR-15 and TTAR-9, and thus more efficient suppression of intermolecular quenching and prevention of pore formation in the first layer. These trends correlate well with the observed monotonic increases in  $J_{SC}$ ,  $V_{OC}$ , and  $\eta$  in series TTAR-9  $\rightarrow$  TTAR-15  $\rightarrow$  TTAR-b8.

## Conclusion

In this work, we designed and synthesized three novel organic sensitizers containing the tetrathienoacene moiety for DSSCs. Their photophysical, electrochemical and photovoltaic properties were investigated. Introduction of a branched 3-methyl-5,5-dimethylhexane group at the TTA unit is favorable in retarding molecular aggregation and suppressing charge recombination through distorting the packing order, and thus achieves the highest cell efficiency of 10.2%. It is found that addition of CDCA has a negative effect on the DSSC photovoltaic performance. By utilizing a three-dimensional photonic crystal layer to increase light absorption, TTAR-b8 exhibits higher short-circuit current densities and achieves a high PCE of 11.2%. This renders TTAR-b8 the best performing fused-thiophene-based organic DSSC dye reported to date.

## Experimental section

### Materials and synthesis

All chemicals and solvents were of reagent grade and obtained from Aldrich, Arco, or TCI Chemical Co. Solvents for reactions

(toluene, benzene, ether, and THF) were distilled under nitrogen from sodium/benzophenone ketyl, and halogenated solvents were distilled from CaH<sub>2</sub>. NMR spectra were measured using a Bruker 300 or 500 MHz spectrometer with chloroform-*d* and/or tetrahydrofuran-*d*<sub>8</sub> as solvents. UV-vis spectra were recorded using a Shimadzu UV3600 UV-vis-NIR spectrophotometer, with EtOH/THF as solvents. Electrospray ionization mass spectrometry was performed using a JMS-700 HRMS spectrometer. Cyclic voltammograms were collected using a CHI 627C electrochemical analyzer (CH Instruments). 2,6-Dibromo-3,7-bis(2,4,4-trimethylpentyl)thieno[2',3':4,5]thieno[3,2-*b*]thieno[2,3-*d*]thiophene (5a), 2,6-dibromo-3,7-dipentadecylthieno[2',3':4,5]thieno[3,2-*b*]thieno[2,3-*d*]thiophene (5b), 2,6-dibromo-3,7-dinonylthieno[2',3':4,5]thieno[3,2-*b*]thieno[2,3-*d*]thiophene (5c), (4-(diphenylamino)phenyl)boronic acid (6), (5-(1,3-dioxolan-2-yl)thiophen-2-yl)tributylstannane (7), and TPA-TTAR (C15)-T-A (2) were synthesized according to the methods reported in the literature.

**Synthesis of 4-(6-bromo-3,7-bis(2,4,4-trimethylpentyl)thieno[2',3':4,5]thieno[3,2-*b*]thieno[2,3-*d*]thiophen-2-yl)-*N,N*-diphenylaniline (6a).** A mixture of (4-(diphenylamino)phenyl)boronic acid (0.318 g, 1.1 mmol), 5a (1.078 g, 1.7 mmol), Pd(PPh<sub>3</sub>)<sub>4</sub> (0.085 g, 5 mol%), and K<sub>2</sub>CO<sub>3</sub> (2 M aqueous solution) (0.608 g, 4.4 mmol) in toluene (40 mL) was stirred and heated to reflux under nitrogen for 4 h. The reaction mixture was poured into water and extracted with dichloromethane, and the combined extracts were washed with brine, then dried over MgSO<sub>4</sub>. The solvent was removed by rotary evaporation, and the crude product was purified by column chromatography on silica gel with dichloromethane/hexane (v/v, 1 : 10) as the eluent to afford 6a as a yellow solid (0.951 g). Yield 70%. <sup>1</sup>H NMR (CDCl<sub>3</sub>, 500 MHz):  $\delta$  7.38–7.02 (m, 14H), 2.85–2.58 (m, 3H), 2.14–2.12 (m, 1H), 1.41–1.0.88 (m, 30H); <sup>13</sup>C NMR (CDCl<sub>3</sub>, 125 MHz):  $\delta$  147.84,

147.56, 142.28, 139.21, 139.19, 131.72, 131.22, 130.91, 129.87, 129.17, 128.70, 128.23, 124.14, 123.33, 122.77, 122.64, 109.05, 51.30, 51.28, 51.05, 38.55, 37.69, 31.14, 29.51, 29.40, 22.58, 22.55, 14.12; HRMS ( $m/z$ , FAB<sup>+</sup>) calcd for C<sub>44</sub>H<sub>48</sub>BrNS<sub>4</sub>: 797.1853; found: 797.1848.

**Synthesis of 4-(6-bromo-3,7-bis(2,4,4-trimethylpentyl)thieno[2',3':4,5]thieno[3,2-*b*]thieno[2,3-*d*]thiophen-2-yl)-*N,N*-diphenylaniline (6c).** A mixture of 4-(diphenylamino)phenylboronic acid (0.318 g, 1.1 mmol), 5c (1.127 g, 1.7 mmol), Pd(PPh<sub>3</sub>)<sub>4</sub> (0.085 g, 5 mol%), and K<sub>2</sub>CO<sub>3</sub> (2 M aqueous solution) (0.608 g, 4.4 mmol) in toluene (40 mL) was stirred and heated to reflux under nitrogen for 4 h. The reaction mixture was poured into water and extracted with dichloromethane, and the combined extracts were washed with brine, then dried over MgSO<sub>4</sub>. The solvent was removed by rotary evaporation, and the crude product was purified by column chromatography on silica gel with dichloromethane/hexane (v/v, 1 : 10) as the eluent to afford 6c as a yellow solid (1.153 g). Yield 82%. <sup>1</sup>H NMR (CDCl<sub>3</sub>, 300 MHz): δ 7.34–7.02 (m, 14H), 2.85–2.73 (m, 4H), 1.78–1.73 (m, 4H), 1.38–0.89 (m, 30H); <sup>13</sup>C NMR (CDCl<sub>3</sub>, 75 MHz): δ 147.94, 147.50, 142.22, 138.79, 135.34, 131.83, 131.37, 129.99, 129.47, 129.28, 128.74, 128.26, 124.94, 124.25, 123.44, 122.87, 122.75, 108.35, 32.02, 29.72, 29.65, 29.52, 29.46, 29.18, 29.10, 28.37, 28.24, 22.82, 14.29; HRMS ( $m/z$ , FAB<sup>+</sup>) calcd for C<sub>46</sub>H<sub>52</sub>BrNS<sub>4</sub>: 825.2166; found: 825.2171.

**Synthesis of 5-(6-(4-(diphenylamino)phenyl)-3,7-bis(2,4,4-trimethylpentyl)thieno[2',3':4,5]thieno[3,2-*b*]thieno[2,3-*d*]thiophen-2-yl)thiophene-2-carbaldehyde (7a).** A mixture of compound 6a (0.583 g, 0.73 mmol), (5-(1,3-dioxolan-2-yl)thiophen-2-yl)tributylstannane (0.392 g, 0.88 mmol) and Pd(PPh<sub>3</sub>)<sub>4</sub> (0.037 g, 5 mol%) in toluene was stirred and heated to reflux for 16 h under nitrogen atmosphere. After cooling to room temperature, the resulting solution was treated with 6 M HCl solution (10 mL) and stirred for 30 min. The solution thus obtained was extracted with dichloromethane and washed with water, then brine solution. The combined organic phases were dried over anhydrous MgSO<sub>4</sub> and removed solvent by rotary evaporation. The obtained crude product was purified using silica gel column chromatography with dichloromethane/hexane (v/v, 3 : 2) as the eluent to give a desired product 7a (0.424 g). Yield 70%. <sup>1</sup>H NMR (CDCl<sub>3</sub>, 500 MHz): δ 9.90 (s, 1H), 7.73 (d, *J* = 3.9 Hz, 1H), 7.37–7.27 (m, 6H), 7.18–7.05 (m, 8H), 2.97–2.21 (m, 3H), 2.22–2.17 (m, 1H), 2.15–2.07 (m, 2H), 1.42–0.88 (m, 29H). This material was insufficiently soluble to obtain a useful <sup>13</sup>C NMR spectrum; HRMS ( $m/z$ , FAB<sup>+</sup>) calcd for C<sub>49</sub>H<sub>51</sub>NOS<sub>5</sub>: 829.2574; found: 829.2582.

**Synthesis of 5-(6-(4-(diphenylamino)phenyl)-3,7-dinonylthieno[2',3':4,5]thieno[3,2-*b*]thieno[2,3-*d*]thiophen-2-yl)thiophene-2-carbaldehyde (7c).** A mixture of compound 6c (0.604 g, 0.73 mmol), (5-(1,3-dioxolan-2-yl)thiophen-2-yl)tributylstannane (0.392 g, 0.88 mmol) and Pd(PPh<sub>3</sub>)<sub>4</sub> (0.037 g, 5 mol%) in toluene was stirred and heated to reflux for 16 h under nitrogen atmosphere. After cooling to room temperature, the resulting solution was treated with 6 M HCl solution (10 mL) and stirred for 30 min. The solution thus obtained was extracted with dichloromethane and washed with water, then brine solution. The combined organic phases were dried over anhydrous MgSO<sub>4</sub> and removed solvent by rotary evaporation. The obtained crude

product was purified using silica gel column chromatography with dichloromethane/hexane (v/v, 3 : 2) as the eluent to give a desired product 7c (0.514 g). Yield 82%. <sup>1</sup>H NMR (CDCl<sub>3</sub>, 300 MHz): δ 9.82 (s, 1H), 7.56 (d, *J* = 3.9 Hz, 1H), 7.39–7.06 (m, 14H), 2.96–2.79 (m, 4H), 1.84–0.98 (m, 35H); <sup>13</sup>C NMR (CDCl<sub>3</sub>, 75 MHz): δ 182.22, 147.62, 147.42, 146.35, 143.21, 142.72, 142.07, 139.45, 136.64, 135.08, 133.52, 131.35, 130.99, 130.53, 130.48, 129.86, 129.55, 129.47, 128.73, 127.95, 127.62, 126.43, 125.53, 124.97, 123.50, 124.97, 123.50, 122.70, 30.99, 29.22, 29.71, 29.63, 29.50, 29.42, 29.12, 28.95, 28.33, 22.78, 14.24; HRMS ( $m/z$ , FAB<sup>+</sup>) calcd for C<sub>51</sub>H<sub>55</sub>NOS<sub>5</sub>: 857.2887; found: 857.2889.

**Synthesis of (E)-2-cyano-3-(5-(6-(4-(diphenylamino)phenyl)-3,7-bis(2,4,4-trimethylpentyl)thieno[2',3':4,5]thieno[3,2-*b*]thieno[2,3-*d*]thiophen-2-yl)thiophen-2-yl)acrylic acid (TPA-TTAR (C8)-TA; 1).** Aldehyde compound 7a (0.183 g, 0.22 mmol), cyanoacetic acid (0.094 g, 1.1 mmol) and piperidine (1.1 mL, 11 mmol) were dissolved in chloroform under a nitrogen atmosphere and heated to reflux for 16 h. After completion of the reaction, the solvent was removed in a vacuum. The residue was extracted with dichloromethane, washed with dil. HCl solution, then with water and dried over anhydrous MgSO<sub>4</sub>. The crude product was purified by column chromatography on silica gel with dichloromethane/methanol (v/v, 9 : 1) as the eluent to yield the desired sensitizer 1 as a reddish brown solid (0.142 g). Yield 72%. <sup>1</sup>H NMR (CDCl<sub>3</sub>, 500 MHz): δ 8.05 (s, 1H), 7.52 (d, *J* = 4.2 Hz, 1H), 7.16–7.07 (m, 6H), 6.97–6.85 (m, 8H), 2.71–2.61 (m, 3H), 2.45–2.38 (m, 1H), 1.96–1.89 (m, 2H), 1.23–0.99 (m, 30H). This material was insufficiently soluble to obtain a useful <sup>13</sup>C NMR spectrum. HRMS ( $m/z$ , FAB<sup>+</sup>) calcd for C<sub>52</sub>H<sub>52</sub>N<sub>2</sub>O<sub>2</sub>S<sub>5</sub>: 896.2632; found: 896.2629. Anal. calcd for C<sub>52</sub>H<sub>52</sub>N<sub>2</sub>O<sub>2</sub>S<sub>5</sub>·2H<sub>2</sub>O: C, 66.92; H, 6.05; N, 3.00. Found: C, 66.8; H, 6.32; N, 3.64.

**Synthesis of (E)-2-cyano-3-(5-(6-(4-(diphenylamino)phenyl)-3,7-dinonylthieno[2',3':4,5]thieno[3,2-*b*]thieno[2,3-*d*]thiophen-2-yl)thiophen-2-yl)acrylic acid (TPA-TTAR (C9)-TA; 3).** Aldehyde compound 7c (0.189 g, 0.22 mmol), cyanoacetic acid (0.094 g, 1.1 mmol) and piperidine (1.1 mL, 11 mmol) were dissolved in chloroform under a nitrogen atmosphere and heated to reflux for 16 h. After completion of the reaction, the solvent was removed in a vacuum. The residue was extracted with dichloromethane, washed with dil. HCl solution, then with water and dried over anhydrous MgSO<sub>4</sub>. The crude product was purified by column chromatography on silica gel with dichloromethane/methanol (v/v, 9 : 1) as the eluent to yield the desired sensitizer 1 as a reddish brown solid (0.153 g). Yield 75%. <sup>1</sup>H NMR (CDCl<sub>3</sub>, 300 MHz): δ 8.18 (s, 1H), 7.68 (d, *J* = 4.2 Hz, 1H), 7.26–7.18 (m, 6H), 7.08–7.01 (m, 8H), 2.92 (t, *J* = 7.9 Hz, 2H), 2.73 (t, *J* = 7.8 Hz, 2H), 1.71–0.76 (m, 36H). This material was insufficiently soluble to obtain a useful <sup>13</sup>C NMR spectrum. HRMS ( $m/z$ , FAB<sup>+</sup>) calcd for C<sub>54</sub>H<sub>56</sub>N<sub>2</sub>O<sub>2</sub>S<sub>5</sub>: 924.2945; found: 924.2948. Anal. calcd for C<sub>54</sub>H<sub>56</sub>N<sub>2</sub>O<sub>2</sub>S<sub>5</sub>·H<sub>2</sub>O: 68.75; H, 6.20; N, 2.97. Found: C, 68.77; H, 6.29; N, 3.11.

### Synthesis and fabrication of three dimensional photonic crystal (3D PhC)

The vertical deposition technique for polystyrene (PS) opal templates is employed to produce the 3D PhC layer.<sup>41</sup> Glass

substrates were placed in vials with deionized water containing between 0.1 and 0.3 vol% PS spheres in suspension, depending on the sphere size and intended opal film thickness. The water was then slowly evaporated at 50 °C in a drying oven. This method yields PS opal films with a controllable thicknesses between 20 and 100 layers and large single crystalline domains, that can be oriented with the (111) planes of the fcc structure parallel to the substrate surface. ZnO was infiltrated into the opal templates by ALD using diethyl zinc (DEtZn) and water (H<sub>2</sub>O) as precursors. The growth temperature was maintained at 85 °C, which is below the glass transition temperature of PS, to avoid deformation or melting of the PS structures. The chamber pressure during the growth was maintained at 10 Torr, and a relatively slow flow of N<sub>2</sub> carrier gas was maintained in the chamber. One ALD reaction cycle consisted of a 1 s exposure to DEtZn followed by a 20 s N<sub>2</sub> purge and a 1 s exposure to H<sub>2</sub>O vapor followed by another 20 s N<sub>2</sub> purge. The PS spheres were then removed by firing the structure in air at 500 °C for 1 h, leaving an ordered fcc array of air holes in the ZnO layer.

### Preparation of photoanode, counter electrode, and DSSCs

0.5 M titanium isopropoxide (TTIP) was added to 0.1 M nitric acid aqueous solution, stirred continually and heated at 88 °C for 8 h. The mixture was transferred to an autoclave (PARR 4540, USA) and heated at 240 °C for 12 h. Eventually, a TiO<sub>2</sub> colloid with an average diameter of 20 nm was obtained. The transparent layer paste (TL paste) was prepared by adding 25 wt% PEG (with respect to the weight of TiO<sub>2</sub> nanoparticles) to the TiO<sub>2</sub> colloid. The scattering layer paste (SL paste) was fabricated by adding 25 wt% PEG and 100 wt% ST-41 (with respect to the weight of TiO<sub>2</sub> nanoparticles) into TiO<sub>2</sub> colloid. Before preparing the TiO<sub>2</sub> photoanode, the fluorine-doped SnO<sub>2</sub> (FTO, TEC-7, 7 Ω sq.<sup>-1</sup>, NSG America, Inc., New Jersey, USA) was cleaned using a neutral cleaner and washed sequentially with deionized water (DIW), acetone, and isopropanol. Then, the compact layer, containing TTIP and 2-methoxyethanol (weight ratio = 1 : 3), was spin-coated on the FTO substrate, to provide a mechanical contact between the FTO and TiO<sub>2</sub> film. Afterwards, a 16 μm porous TiO<sub>2</sub> film, consisting of 12 μm TL and 4 μm SL, was coated on the treated FTO using the doctor-blade technique. Each TiO<sub>2</sub> layer was sintered at 500 °C for 30 min in an oxygen atmosphere. The FTO glass with the TiO<sub>2</sub> film was immersed in a 5 × 10<sup>-4</sup> M TTAR series dye solution, which was dissolved in DCM/ACN/tBA (v/v/v = 8/1/1) at room temperature for 24 h to obtain the photoanode for a DSSC. The counter electrode (CE) was prepared by sputtering Pt on the FTO substrate. The deposition time was set at 20 s under a sputter current of 40 mA. Herein, the DSSC was composed of the TiO<sub>2</sub> photoanode with the CE, and the gap between those two electrodes was sealed by heating a 25 μm Surlyn® film. Finally, the electrolyte, which contained 0.1 M GuSCN, 1.2 M DMPII, 0.035 M I<sub>2</sub>, and 0.5 M tBP in ACN/MPN (volume ratio of 8 : 2), was injected into the cell gap between the two electrodes *via* capillary action.

### Characterization

A Newport-Oriel® IQE-200 ACDC was used to measure incident photon to charge carrier efficiency (IPCE). The devices were evaluated under 100 mW cm<sup>-2</sup> AM1.5 G simulated sunlight with a class A solar cell analyzer (Spectra Nova Tech.). A silicon solar cell fitted with a KG3 filter tested and certified by the National Renewable Energy Laboratory (NREL) was used for calibration. The KG3 filter accounts for the different light absorption between the DSSC and the silicon solar cell, and it ensures that the spectral mismatch correction factor approaches unity.

### Acknowledgements

This research is supported in part by the ANSER Center, an Energy Frontier Research Center funded by the U.S. DOE-BES (DE-SC0001059). We thank the NSF-MRSEC program through the Northwestern University Materials Research Science and Engineering Center (DMR-1121262) for the support of the X-ray Diffraction Facility. This work is also supported in part by the Ministry of Science and Technology (MOST) of Taiwan, under grant number MOST 103-2119-M-007-012.

### References

- 1 B. O'Regan and M. Grätzel, *Nature*, 1991, **353**, 737–740.
- 2 U. Bach, D. Lupo, P. Comte, J. E. Moser, F. Weissortel, J. Salbeck, H. Spreitzer and M. Grätzel, *Nature*, 1998, **395**, 583–585.
- 3 M. Grätzel, *Inorg. Chem.*, 2005, **44**, 6841–6851.
- 4 A. Hagfeldt and M. Grätzel, *Acc. Chem. Res.*, 2000, **33**, 269–277.
- 5 S. Mathew, A. Yella, P. Gao, R. Humphry-Baker, F. E. Curchod, N. Ashari-Astani, I. Tavernelli, U. Rothlisberger, K. Nazeeruddin and M. Grätzel, *Nat. Chem.*, 2014, **6**, 242–247.
- 6 S. Shalini, R. Balasundaraprabhu, T. S. Kumar, N. Prabavathy, S. Senthilarasu and S. Prasanna, *Int. J. Energy Res.*, 2016, **40**, 1303–1320.
- 7 V. Sugathan, E. John and K. Sudhakar, *Renewable Sustainable Energy Rev.*, 2015, **52**, 54–64.
- 8 A. Hagfeldt, G. Boschloo, L. Sun, L. Kloo and H. Pettersson, *Chem. Rev.*, 2010, **110**, 6595–6663.
- 9 Y. Jiao, F. Zhang, M. Grätzel and S. Meng, *Adv. Funct. Mater.*, 2013, **23**, 424–429.
- 10 E. Kozma, I. Concina, A. Braga, L. Borgese, L. E. Depero, A. Vomiero, G. Sberveglieri and M. Catellani, *J. Mater. Chem.*, 2011, **21**, 13785–13788.
- 11 S. Qu, W. Wu, J. Hua, C. Kong, Y. Long and H. Tian, *J. Phys. Chem. C*, 2010, **114**, 1343–1349.
- 12 J. He, W. Wu, J. Hua, Y. Jiang, S. Qu, J. Li, Y. Long and H. Tian, *J. Mater. Chem.*, 2011, **21**, 6054–6062.
- 13 D. Kim, A. Ghicov, S. P. Albu and P. Schmuki, *J. Am. Chem. Soc.*, 2008, **130**, 16454–16455.
- 14 F. Sauvage, F. Di Fonzo, A. Li Bassi, C. S. Casari, V. Russo, G. Divitini, C. Ducati, C. E. Bottani, P. Comte and M. Grätzel, *Nano Lett.*, 2010, **10**, 2562–2567.

- 15 J. Yang, P. Ganesan, J. Teuscher, T. Moehl, Y. J. Kim, C. Yi, P. Comte, K. Pei, T. W. Holcombe, M. K. Nazeeruddin, J. Hua, S. M. Zakeeruddin, H. Tian and M. Grätzel, *J. Am. Chem. Soc.*, 2014, **136**, 5722–5730.
- 16 Z. Yao, M. Zhang, H. Wu, L. Yang, R. Li and P. Wang, *J. Am. Chem. Soc.*, 2015, **137**, 3799–3802.
- 17 H. Chen, H. Huang, X. Huang, J. N. Clifford, A. Forneli, E. Palomares, X. Zheng, L. Zheng, X. Wang, P. Shen, B. Zhao and S. Tan, *J. Phys. Chem. C*, 2010, **114**, 3280–3286.
- 18 H. Choi, I. Raabe, D. Kim, F. Teocoli, C. Kim, K. Song, J.-H. Yum, J. Ko, M. K. Nazeeruddin and M. Grätzel, *Chem.–Eur. J.*, 2010, **16**, 1193–1201.
- 19 D. P. Hagberg, T. Marinado, K. M. Karlsson, K. Nonomura, P. Qin, G. Boschloo, T. Brinck, A. Hagfeldt and L. Sun, *J. Org. Chem.*, 2007, **72**, 9550–9556.
- 20 S. Haid, M. Marszalek, A. Mishra, M. Wielopolski, J. Teuscher, J.-E. Moser, R. Humphry-Baker, S. M. Zakeeruddin, M. Grätzel and P. Bäuerle, *Adv. Funct. Mater.*, 2012, **22**, 1291–1302.
- 21 D. Joly, L. Pellejà, S. Narbey, F. Oswald, J. Chiron, J. N. Clifford, E. Palomares and R. Demadrille, *Sci. Rep.*, 2014, **4**, 4033.
- 22 B.-G. Kim, K. Chung and J. Kim, *Chem.–Eur. J.*, 2013, **19**, 5220–5230.
- 23 C. Teng, X. Yang, C. Yang, S. Li, M. Cheng, A. Hagfeldt and L. Sun, *J. Phys. Chem. C*, 2010, **114**, 9101–9110.
- 24 J. Youn, P.-Y. Huang, Y.-W. Huang, M.-C. Chen, Y.-J. Lin, H. Huang, R. P. Ortiz, C. Stern, M.-C. Chung, C.-Y. Feng, L.-H. Chen, A. Facchetti and T. J. Marks, *Adv. Funct. Mater.*, 2012, **22**, 48–60.
- 25 C. Kim, M.-C. Chen, Y.-J. Chiang, Y.-J. Guo, J. Youn, H. Huang, Y.-J. Liang, Y.-J. Lin, Y.-W. Huang, T.-S. Hu, G.-H. Lee, A. Facchetti and T. J. Marks, *Org. Electron.*, 2010, **11**, 801–813.
- 26 N. Zhou, K. Prabakaran, B. Lee, S. H. Chang, B. Harutyunyan, P. Guo, M. R. Butler, A. Timalina, M. J. Bedzyk, M. A. Ratner, S. Vegiraju, S. Yau, C.-G. Wu, R. P. H. Chang, A. Facchetti, M.-C. Chen and T. J. Marks, *J. Am. Chem. Soc.*, 2015, **137**, 4414–4423.
- 27 D. Joly, M. Godfroy, L. Pelleja, Y. Kervella, P. Maldivi, S. Narbey, F. Oswald, E. Palomares and R. Demadrille, *J. Mater. Chem. A*, 2017, **5**, 6122–6130.
- 28 J.-H. Yum, T. W. Holcombe, Y. Kim, K. Rakstys, T. Moehl, J. Teuscher, J. H. Delcamp, M. K. Nazeeruddin and M. Grätzel, *Sci. Rep.*, 2013, **3**, 2446.
- 29 Y. Numata, I. Ashraful, Y. Shirai and L. Han, *Chem. Commun.*, 2011, **47**, 6159–6161.
- 30 S. Paek, H. Choi, H. Choi, C.-W. Lee, M.-s. Kang, K. Song, M. K. Nazeeruddin and J. Ko, *J. Phys. Chem. C*, 2010, **114**, 14646–14653.
- 31 W. L. Vos, R. Sprik, A. van Blaaderen, A. Imhof, A. Lagendijk and G. H. Wegdam, *Phys. Rev. B: Condens. Matter Mater. Phys.*, 1996, **53**, 16231.
- 32 B. Lee, D.-K. Hwang, P. Guo, S.-T. Ho, D. B. Buchholtz, C.-Y. Wang and R. P. H. Chang, *J. Phys. Chem. B*, 2010, **114**, 14582–14591.
- 33 B. Lee, P. Guo, S.-Q. Li, D. B. Buchholz and R. P. H. Chang, *ACS Appl. Mater. Interfaces*, 2014, **6**(20), 17713–17722.
- 34 S. R. Raga, E. M. Barea and F. Fabregat-Santiago, *J. Phys. Chem. Lett.*, 2012, **3**, 1629–1634.
- 35 G. Li, M. Liang, H. Wang, Z. Sun, L. Wang, Z. Wang and S. Xue, *Chem. Mater.*, 2013, **25**, 1713–1722.
- 36 J. van de Lagemaat, N. G. Park and A. J. Frank, *J. Phys. Chem. B*, 2000, **104**, 2044–2052.
- 37 M. Lu, M. Liang, H.-Y. Han, Z. Sun and S. Xue, *J. Phys. Chem. C*, 2011, **115**, 274–281.
- 38 S. H. Chang, C.-H. Chiang, H.-M. Cheng, C.-Y. Tai and C.-G. Wu, *Opt. Lett.*, 2013, **38**, 5342–5345.
- 39 M. J. Giriffith, M. James, G. Triani, P. Wagner, G. G. Wallace and D. L. Officer, *Langmuir*, 2011, **27**, 12944–12950.
- 40 L. G. Parratt, *Phys. Rev.*, 1954, **95**, 359–369.
- 41 *Handbook of Crystal Growth*, Elsevier, Boston, 2nd edn, 2015, pp. 1157–1182.